Radiation Physics and Chemistry 196 (2022) 110097

Contents lists available at ScienceDirect

Radiation Physics and Chemistry

journal homepage: www.elsevier.com/locate/radphyschem

Radicals in ammonium tartrate at 295 K by X-radiation: Revised radical structures by EMR and DFT analyses

Einar Sagstuen [a,*], Veronika Kugler [a,b,1], Eli Olaug Hole [a], Anders Lund [b]

[a] Department of Physics, University of Oslo, 0316, Oslo, Norway
[b] Department of Physics, Chemistry and Biology, Linköping University, 581 83, Linköping, Sweden

ARTICLE INFO

Keywords:
Electron paramagnetic resonance
Electron magnetic resonance
Ammonium tartrate
Radiation induced radicals
Ionizing radiation
EPR dosimetry
Periodic DFT

ABSTRACT

The simple amino acid l-α-alanine (*ala*) in polycrystalline form was among the first substances to be proposed and subsequently developed for Electron Paramagnetic Resonance (EPR)-based solid state radiation dosimetry. One disadvantage with *ala* is a relatively low sensitivity for doses below a few gray (Gy) which is a dose range of particular interest in medical, accident and environmental applications. A number of other compounds have been screened and some of these have shown a better sensitivity to radiation exposure than *ala*, in some cases up to a factor of 7–8. In particular ammonium tartrate (AT) and lithium formate (LiFo) have been taken into practical use. The present work was initially aimed to investigate the low-temperature radical products in AT, and the reactions leading to the product of dosimetric interest at room temperature. As a part of these studies, the previously characterized major room temperature radical product was re-investigated using single crystal electron magnetic resonance (EMR) techniques combined with periodic density functional theory (DFT) -type quantum chemical calculations. Surprisingly, this study showed that the molecular structure of the dominant radical at room temperature is somewhat different from that previously proposed. Furthermore, a second room temperature radical, previously not well characterized, was carefully investigated and three hyperfine coupling tensors were determined. These three tensors were sufficient to simulate all experimental observations for the second radical but not alone sufficient to permit an unambiguous molecular structure of the defect to be determined. It appears that the EPR resonance from this radical does not influence the dosimetric potential of AT.

1. Introduction

Electron Paramagnetic Resonance (EPR) spectroscopy has during the last 3-4 decades gained acceptance as a precise radiation dosimetry system within a range of physical, biological, medical and industrial applications (Ikeya, 1993). The amino acid l-α-alanine (*ala*) in polycrystalline form was among the first substances to be proposed and subsequently developed for this purpose. Major reasons for this were a very high radical yield and an unusual long lifetime of the major radical formed upon radiation exposure at room temperature (Bradshaw et al., 1962; Hansen et al., 1987; Regulla and Deffner, 1982; Wieser et al., 1989). Since EPR measurements are non-destructive, this longevity of the induced radicals suggested additional benefits like cumulative radiation measurement procedures and long-time dosimeter storage for quality control and metastudies. One disadvantage with *ala*, however, is a relatively low sensitivity for doses below a few grays which is a dose range of interest for many possible applications, in particular for medical and environmental purposes.

For these reasons, a number of other compounds have been screened and many of these have, to variable extent, been further explored as possible alternatives to *ala* for low-dose applications. A few of these have shown a better sensitivity to radiation exposure than *ala*, in some cases up to a factor of 7–8. In particular, ammonium tartrate (AT) and lithium formate (LiFo) have been taken into practical use (Adolfsson et al., 2014; Bartolotta et al., 2001; Brustolon et al., 1999; Gustafsson et al., 2004; Lund et al., 2002, 2005; Malinen, 2014; Marrale et al., 2006, 2009; Olsson et al., 1999, 2000; Polat and Korkmaz, 2009; Vestad et al., 2003).

The detailed characterization of the molecular structure of the radiation induced radical(s), and the understanding of the radiation chemistry initiated by the primary ionization events in these compounds, have in some cases proved useful and of importance for the dosimetry measurement procedures. The room temperature EPR signal

* Corresponding author.
E-mail addresses: einar.sagstuen@fys.uio.no (E. Sagstuen), e.o.hole@fys.uio.no (E.O. Hole), anders.lund@liu.se (A. Lund).
[1] Current address: Carl Zeiss Microscopy Ltd, Cambridge, UK. kugler@email.com

https://doi.org/10.1016/j.radphyschem.2022.110097
Received 9 November 2021; Received in revised form 4 February 2022; Accepted 21 March 2022
Available online 30 March 2022

from *ala* has been shown to originate from (at least) three different radical species, and for precise measurements this fact should in some cases be considered (Heydari et al., 2002; Sagstuen et al., 1997). LiFo exhibits only one major radical at room temperature, but several other radicals, occurring in minor amounts, do to some extent disturb the main signal (Krivokapic et al., 2015; Vestad et al., 2004). Not much is published regarding radiation products in AT; a study of the main radical being of dosimetric interest at room temperature (Brustolon et al., 1996) and a more recent study of one minority species (Brustolon et al., 1996, 2015). In addition, a peculiar slow increase of the EPR signal of dosimetric interest immediately after irradiation at room temperature (Olsson et al., 2000) suggests that slow radical reactions leading to this product take place. For this reason, a recommended practice for using AT as an EPR dosimeter is to wait at least 6 h after room temperature irradiation before measurements, thus allowing for the secondary reactions to complete.

The present work was initiated to investigate the low-temperature radical products and their reactions leading to the room temperature products in AT. As a part of this study, the major room temperature radical product (hereafter called radical **R1**), previously characterized by Brustolon et al. (1996), was re-investigated using single crystal X-band EPR, electron-nuclear double resonance (ENDOR) and ENDOR-induced EPR (EIE) techniques combined with advanced quantum chemical calculations.

As commented above, a second radical in AT at room temperature was previously observed and attempted analyzed (Brustolon et al., 2015). From these data, it might appear that this second resonance exhibit some overlap with the **R1** radical resonance and hence might disturb the dosimetric properties of AT. In the present work, the second radical (hereafter designated radical **R2)** was therefore carefully investigated and three hyperfine coupling tensors were determined. These three tensors were sufficient to simulate all experimental observations for **R2**.

In the present work, it is shown that the molecular structure of the **R1** radical is different from that proposed previously. Furthermore, the major proton coupling of the **R2** radical is demonstrated to be sufficiently large for the **R2** resonance not to overlap the major resonance, used for dosimetry purposes, to any significant degree. Due to the novelty of these results, this reinvestigation of room temperature radicals in AT is reported here separately, while the results from the low-temperature part of the project will be published elsewhere.

2. Experimental and calculational methods

Di-ammonium tartrate (AT), $H_4N^+\cdots{}^-OOC1\text{-}C2HOH\text{–}C3HOH\text{–}C4OO^-\cdots NH_4^+$, carbon atoms numbered according to the crystal structure analysis, was obtained from Sigma-Aldrich Co, and used without further purification. Single crystals were grown from aqueous solutions by slow evaporation at room temperature. Partially deuterated crystals (all easily exchangeable nitrogen- and oxygen bonded protons substituted by deuterons) were obtained similarly using 99.9% heavy water (Cambridge Isotope Laboratory) by 2–3 recrystallizations. The structure of AT crystals has been determined using X-ray diffraction methods (Yadava and Padmanabhan, 1973) and shown to be monoclinic with space group $P2_1$ and two molecular units in the unit cell (one of these units is shown in Fig. 1). The lengths of the unit cell axes were determined to be $a = 0.7083$, $b = 0.6128$, and $c = 0.8808$ nm, and the monoclinic angle to $\beta = 92.42°$. In that work the proton coordinates were not determined. However, the same authors subsequently published a neutron diffraction analysis (Yadava and Padmanabhan, 1976) where the proton coordinates also were established. In the present work, the coordinates resulting from the neutron diffraction analysis were used exclusively for the data analyses and radical structure modelling. All interatomic directions used for comparison with experimental data are reproduced in Table S1 (Section 2, Supplemental Information).

The experimental procedures differed somewhat for the **R1** and **R2** radicals due to the use of two different spectrometer systems. All technical details for these procedures are presented in Section 1, Supplemental Information.

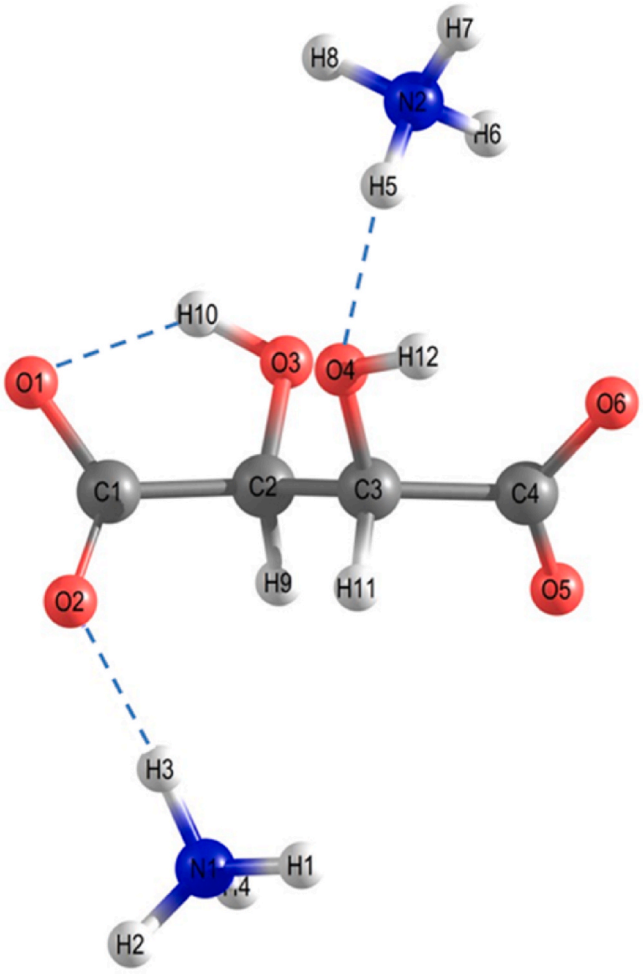

Fig. 1. The di-ammonium tartrate structural unit in the crystalline state. The crystal unit cell contains two of these structures. Dashed lines indicate intra-unit hydrogen bonds. Atomic numbering is as defined in the neutron diffraction study (Yadava and Padmanabhan, 1976).

EPR and ENDOR measurements were performed by using the three crystallographic axes *a*, *b* and c as rotation axes, rotating the crystals in steps of 10 or 5°, respectively. An orthogonal *a*bc* system was chosen as reference axis system ($\underline{a}^* = \underline{b}$ x $\underline{c}$). Proton hyperfine coupling (hfc) tensors were extracted from experimental ENDOR data using the program MAGRES (Nelson, 1980; Nelson and Nave, 1981; Sagstuen et al., 2000). With two exceptions, the high-frequency ENDOR lines were used for the data analyses. The exceptions were for resonances **R1**(3) and **R2** (3) (see below) where the low-frequency lines were used. EIE spectra were recorded at selected crystal orientations and at selected ENDOR lines at each of these orientations. This allowed a determination of which ENDOR resonance lines belong to which radical in the sample and also the EPR absorption-like pattern from this radical.

Schonland (1959) pointed out an inherent two-fold ambiguity in g- and hfc-tensors determined by e.g. crystal rotations in three crystallographic planes, due to an ambiguity of the signs of the off-diagonal tensor elements. This ambiguity may be solved experimentally in a number of ways (Vrielinck et al., 2008). In the present work, the Schonland ambiguity was not experimentally solved for the hfc tensors since for these β- and γ-type coupling tensors the two different Schonland solutions were very similar and all conclusions made below are valid regardless of the choice of signs of the off-diagonal tensor

elements. The tensors reported in Tables 1 and 3 and Table S2 (Section 2, Supplemental Information) are those obtained from the experimental data.

For the EPR spectral simulations the program KVASAT was used, a program which includes microwave power saturation effects in the EPR spectra (Sagstuen et al., 2000).

All reported DFT calculations were performed using the CP2K program (The CP2K developers group, 2011) in a periodic approach. A periodic unit containing 16 AT molecular units with a total of 384 atoms, consisting of the crystallographic unit cell duplicated once in each of the three crystallographic directions [2*a*2*b*2*c*], was used in order to prevent interactions between the periodic images of the radical. The neutron diffraction crystal data were used for the initial set of atomic coordinates. Calculations were performed at two different levels of theory (LOT). In the first approach the Gaussian and Plane Wave (GPW) method (Lippert et al., 1999) was used to get a first estimate of the geometrical structures. In these calculations, Goedecker-Teker-Hutter (GTH) pseudo potentials (Goedecker et al., 1996; Hartwigsen et al., 1998; Krack, 2005) were used along with a TZVP-GTH basis set (VandeVondele and Hutter, 2007) and the BLYP functional (Becke, 1988; Lee et al., 1988). The cutoff for the plane wave basis was 400 Rydberg (Ry). The initial periodic unit was optimized and the resulting set of atomic coordinates was used as input for the radical structure optimizations. The final results were obtained by subsequent geometry optimizations and hfc tensor calculations at the all-electron Gaussian and Augmented Plane Wave (GAPW) approach (Krack and Parrinello, 2000; Lippert et al., 1999) in order to explicitly describe the core electrons. For these calculations a plane wave cutoff of 400 Ry was used along with an all-electron TZVP basis set (Godbout et al., 1992) and the BLYP functional. For all calculations the atomic spin distribution was estimated by Mulliken population analysis. For modelling radical **R1** (see below), two initial radical structures *R1-I* and *R1-II* were created by simply eliminating the C3- and C2 hydrogen atoms, respectively, from the pristine structures. The *R1-II* model is the structure of the major radical in AT at room temperature proposed by Brustolon et al. (1996). No geometrical constraints were employed for any of the final calculations.

3. Results and discussion

The room temperature EPR spectra from x-irradiated crystalline AT are well known from the literature (Brustolon et al., 1996). The major resonance most often appears as a doublet with pronounced shoulders, whereas both singlet and triplet patterns are observed at some orientations. Fig. 2 shows 1st derivative EPR spectra recorded along the *a**, *b* and *c** axes. These data illustrate the major resonance features due to the **R1** radical (dashed and dotted lines), and the EPR spectra also depict the weak outer features that do not belong to the **R1** radical and to date only are poorly characterized (Brustolon et al., 2015). Even weaker features, most probably due to radicals with naturally occurring ^{13}C nuclei (I = 1/2) (Brustolon et al., 1996), could be observed on the outside of the weak outer features in Fig. 2. These have not been investigated in the present work. It should be noted that the EPR and ENDOR spectra appears to be similar regardless if the crystals have been irradiated at 275 K or at 6 K with subsequently annealing at 295 K.

ENDOR spectra were recorded off one of the main central resonance lines for the major radical **R1**, while one of the weaker high field EPR features was monitored for ENDOR analyses of the minority radical **R2** (see Fig. 4). Fig. 2 also includes the absorption-like EIE spectra from the **R1** radical along the *b* and *c** axes. Note that these EIE spectra were recorded off a **R1** radical ENDOR line at 12.5 mW and microwave saturation effects are therefore significantly present in these spectra. In particular, the pair of features in the EPR spectra marked with dotted lines are due to distant proton dipolar interactions ("spin flip" lines) and are strongly power-enhanced in the absorption-like EIE spectra (Sagstuen et al., 2000).

3.1. Major radical (*R1*)

For radical **R1**, the ENDOR spectra were similar to those previously published (Brustolon et al., 1996). Three main ENDOR lines were observed and followed and in Fig. S1 (Section 3, Supplemental Information) the ENDOR line variation diagram for the three planes of rotation is shown. These data were used to extract three proton hyperfine coupling tensors which are presented in Table 1. The fully drawn lines in Fig. S1 are calculated from these hyperfine coupling tensors.

In partially deuterated crystals, the ENDOR lines associated with hyperfine couplings **R1**(2) and **R1**(3) were either absent or of low intensity, and were thus assigned to couplings with easily exchangeable protons, *i.e.* the H(-OH) or H(NH_4^+) protons.

Coupling **R1**(1) exhibits a dipolar coupling tensor similar to that for a carbon-bonded β-proton coupling, whereas **R1**(3) is characteristic for an oxygen-bonded β-proton coupling (Sagstuen et al., 2012). **R1**(2), due to its exchangeability and its significantly smaller dipolar coupling, must be ascribed to an oxygen-bonded γ-proton coupling. Hence, these three interactions are most probably due to a radical fragment … $–CH_\beta(OH_\gamma)–\bullet C(OH_\beta)–$ … in the tartrate backbone.

Although the principal values of the hyperfine coupling tensor in Table 1 agree fairly well with the previous work by Brustolon and coworkers (Brustolon et al., 1996), the eigenvectors do not agree. These authors concluded that the radical was formed by a net H-abstraction

Table 1
Experimental hyperfine coupling tensors (in MHz) for radical **R1** in crystals of ammonium tartrate x-irradiated at 275 K. δ is the angle of deviation (°) between the respective eigenvector and the specific C ⋯ H directions as indicated in Footnote 1. See text for the choice of Schonland combination and signs of the eigenvector components. Hyperfine interactions being absent or only weakly present in partially deuterated crystals are indicated by (exch.). Uncertainties are quoted at the 95% confidence level in the last digit(s) of the corresponding number.

Tensor	Principal value	Isotropic value	Dipolar coupling	a*	b	c	δ
R1(1)	14.90(4)		9.31(6)	0.313(4)	0.295(5)	−0.903(8)	7.5[a]
	2.81(9)	5.59(4)	−2.87(10)	0.807(3)	−0.584(7)	0.089(5)	
	−0.94(8)		−6.38(9)	0.501(1)	0.756(5)	0.421(2)	
R1(2)	12.99(3)		5.23(4)	0.227(4)	0.959(4)	−0.169(3)	24.9[b]
(exch.)	6.52(3)	7.76(2)	−1.24(4)	0.648(1)	−0.019(3)	0.761(3)	
	3.77(3)		−3.99(4)	0.727(4)	−0.282(3)	−0.626(3)	
R1(3)	9.31(7)		16.65(8)	0.509(1)	0.432(10)	−0.744(1)	34.0[c]
(exch.)	−14.29(6)	−7.34(4)	−6.95(7)	0.704(11)	−0.706(10)	0.072(2)	
	−17.04(7)		−9.70(8)	0.494(12)	0.561(9)	0.664(1)	

[1]Crystallographic directions (see also Table S1, Supplementary Information):a) C3 – HOC3 (**R1**(3)) −0.2358 0.0319 0.9713 .b) C3 – HOC2 (**R1**(2)) −0.1585 0.9197 −0.3591 .c) C3 – HC2 (**R1**(1)) 0.1972 0.2513 −0.9476 .

Table 2
Final DFT-calculated proton hfc tensors (in MHz) for the HC3-abstraction radical model *R1-I* of radical **R1** in crystals of ammonium tartrate. Deviations **δ** (in °) between a given eigenvector and its experimental counterpart (see Table 1) are given in the last column.

Tensor	Principal value	Isotropic value	Dipolar coupling	a*	b	c	δ
HC2	11.34		8.28	−0.2968	−0.2500	0.9216	3.1
	−0.38	3.06	−3.44	−0.7385	0.6720	−0.0555	6.6
	−1.78		−4.84	0.6055	0.6971	0.3841	7.3
HOC2	13.81		6.06	−0.2451	−0.9660	0.0824	4.8
	6.45	7.75	−1.30	0.6013	−0.0848	0.7945	4.1
	2.99		−4.76	−0.7605	0.2442	0.6017	3.2
HOC3	9.52		17.64	−0.4395	−0.4273	0.7901	4.8
	−15.67	−8.12	−7.55	−0.7853	0.6099	−0.1069	7.6
	−18.22		−10.10	0.4362	0.6674	0.6036	7.7

Table 3
Experimental hyperfine coupling tensors (in MHz) for radical **R2** in crystals of ammonium tartrate x-irradiated at 6 K and annealed/measured at 295 K. δ is the angle of devation (°) between the respective eigenvector and the crystallographic C ⋯ H direction indicated in the footnote. See text for the choice of Schonland combination and sign of the eigenvector components. Hyperfine interactions not present in partially deuterated crystals are indicated by (exch.). Uncertainties are quoted at the 95% confidence level in the last digit(s) of the corresponding number.

Tensor	Principal value	Isotropic value	Dipolar value	Eigenvector			δ
				a*	b	c	
R2(1)	91.62(3)		6.87(3)	0.197(1)	−0.900(11)	−0.388(5)	7.5[a]
	81.80(2)	84.75 (1)	−2.95(2)	0.427(1)	−0.278(4)	0.861(3)	
	80.84(2)		−3.91(2)	0.883(1)	0.335(4)	−0.330(11)	
R2(2)	26.30(3)		7.36(4)	0.132(2)	−0.981(5)	−0.139(5)	
	15.73(3)	18.94(2)	−3.21(4)	0.663(0)	−0.017(1)	0.749(2)	
	14.79(3)		−4.15(4)	0.737(2)	0.191(5)	−0.648(5)	
R2(3) (exch.)	5.57(20)		13.22(21)	−0.102(5)	0.994(7)	0.047(3)	17.6[b]
	−13.40(3)	−7.65(7)	−5.75(8)	0.397(1)	−0.003(3)	0.918(5)	
	−15.11(3)		−7.46(8)	0.912(2)	0.113(3)	−0.394(7)	

[1]Crystallographic directions (see also Table S1 in Section 2, Supplemental Information):a) C2 – HC3 0.2357 −0.8372 0.4935 .b) C2 – HOC2 −0.3929 0.9194 −0.0209 .

from the tartrate C2-position (see atomic numbering in Fig. 1). However, comparing the eigenvectors for the various hyperfine couplings in Table 1 with those in Table 1 in the previous work (Brustolon et al., 1996), it appears that the *a** and *c*-axes components in the previous work are interchanged. Furthermore, examining in detail the line plots presented in Fig. 4 of the previous work (Brustolon et al., 1996), inconsistencies in axes assignments are clearly evident. Apparently, the *a**- and *c*-axes designations in the left panel of Fig. 4 (Brustolon et al., 1996) somehow have been interchanged. For that reason, the present data were carefully re-examined in combination with new rotation experiments aided by x-diffraction determinations of the crystal axes. From this it was concluded that the data in Table 1 above, the data in Fig. S1 (Section 3, Supplemental Information) and Fig. 2 are correct. Fig. S2 (Section 3, Supplemental Information) show simulated **R1**-radical EPR spectra using the data in Table 1. It follows from the data in Table 1 that radical **R1** most reasonably should be ascribed to a radical formed by net H-abstraction from the tartrate C3-position (see atomic numbering in Fig. 1) and not from the C2-position as previously proposed.

3.2. DFT calculations for radical *R1*

Two radical models were created in our attempts to reproduce the experimental hyperfine coupling data for radical **R1**. These two models are designated *R1-I* and *R1-II*. Model *R1-I* was formed by removing the hydrogen atom bonded to C3, whereas model *R1-II* was formed by removing the hydrogen atom bonded to C2. All DFT calculations were made as described in Section 2 above. The major results from the final DFT calculations for model *R1-I* (HC3-abstraction) are shown in Table 2. These data are directly comparable with the experimental data in Table 1.

Table S3 (Section 3, Supplemental Information) shows the results from the calculations made for model *R1-II* (HC2-abstraction). The experimental data identical to those in Table 1 are for convenience reproduced in Table S2 (Section 3, Supplemental Information). The data shown in Tables 1 and 2 and the data in Tables S2 and S3 (Section 3, Supplemental Information) demonstrate clearly the excellent agreement between the experimental results for **R1** and the calculated hyperfine coupling tensors for model *R1-I*. On the other hand, a substantial mismatch for the *R1-II* radical model with the **R1** experimental data is evident. These results provide definitive support for the structural assignment of radical **R1** in AT as an H(C3) abstraction radical.

Fig. 3 shows the DFT optimized molecular unit of Fig. 1 and the two optimized radical models *R1-I* and *R1-II* within the freely optimized periodic cell of 384 atoms.

3.3. Minority radical (*R2*)

The weaker lines on each flank of the central major radical resonance lines in Fig. 2 are due to a minority radical species (radical **R2**) which, in spite of its relatively low abundance, has triggered some interest in the literature (Brustolon et al., 2015). In general, these flanking resonance lines are weak, and high-sensitivity settings of the ENDOR experiment were required to allow for a detailed characterization of the resonance.

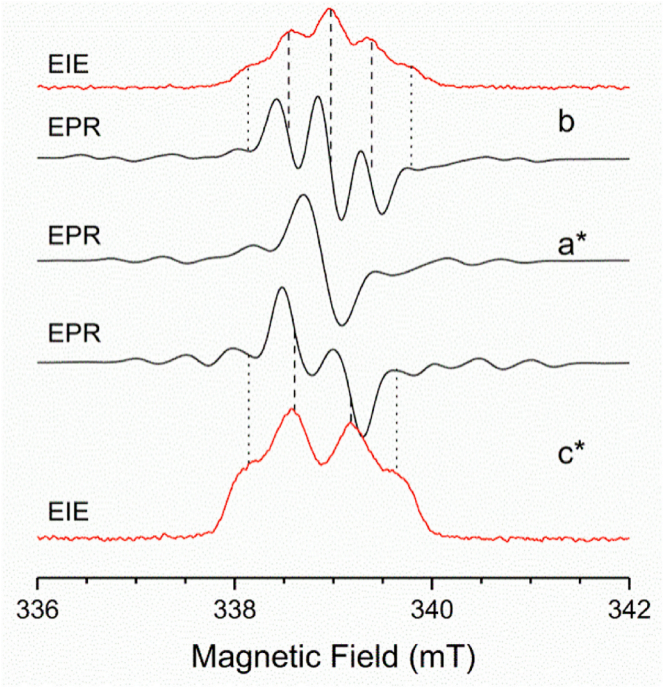

Fig. 2. Experimental EPR and EIE (in red) spectra from crystals of ammonium tartrate X-irradiated at 275 K and measured at 295 K or 250 K, respectively. All spectra have been normalized to a common resonance frequency 9496.00 MHz. The crystal orientations relative to the external magnetic field are given. The microwave power level incident to the cavity was 0.5 mW for the EPR spectra, and 12.5 mW for the EIE spectra. The EIE spectra were recorded off **R1**-radical ENDOR lines (strong central features in the EPR spectra) and will therefore not show features due to other radicals present in the EPR spectra (see Fig. 4). Vertical dashed and dotted lines are included for visual aid only (see text).

For the ENDOR spectra, the magnetic field usually was locked at about 340 mT (see Fig. 4), at the most prominent peak on the high-field side of the **R1** resonance. This position is marked by an arrow in panel C of Fig. 4.

Upon sweeping the radiofrequency (rf) from 16 MHz and upwards, 4 ENDOR lines were observed for the rot plane (no site splitting for rotation about the monoclinic axis). These were assigned to three different proton hyperfine couplings, designated **R2**(1), **R2**(2) and **R2**(3). For coupling **R2**(1), both the high-frequency **R2**(1+) and low-frequency **R2**(1-) lines were observed for rot, however, the low-frequency line R2(1-) intensity was too weak to be clearly observed in the other two planes. For **R2**(3), the resonance line appearing near 21 MHz in Fig. 4A turned out to be the low-frequency **R2**(3-) branch of the pair of ENDOR lines associated with this hyperfine interaction. The **R2**(3+) branch was observed occasionally, but the ENDOR lines were generally too weak to be followed in detail. The same was true for the **R2**(2-) line. The line assignments above were supported by the EIE spectrum rf sweep directions for the different ENDOR lines. For the low-frequency ENDOR **R2**(1-) line in Fig. 4A, the rf was swept in opposite direction to the magnetic field. This is a necessity for the case of the low-frequency ENDOR branch of a coupling with $a > 2\ \nu_p$ (where a is the actual value of hyperfine coupling constant at that given orientation in the field). With increasing magnetic field B, $\nu_p = g_N\beta_N B$ increases and the value of the low-frequency ENDOR line position, at about $a/2$- ν_p, *decreases*. To have the ENDOR line in lock position during the magnetic field sweep, the rf must be therefore swept slowly downwards during the upwards magnetic field sweep, and not upwards as common for the other ENDOR lines.

Support for these line assignments were also obtained by the ENDOR spectrum simulation by exact diagonalization methods using the EasySpin toolbox (Stoll and Schweiger, 2006), see Fig. 4B. For this simulation, the hfc tensor data in Table 3 were used. The agreement between the experimental and calculated line positions is excellent. Minor deviations, less than 0.09 MHz for the high- and low-frequency line positions due to **R2**(2+) and **R2**(3-) and about 0.25 MHz for the **R2**(1+) and **R2**(1-) resonance line positions in the simulated spectrum, were observed. The latter result indicates that the high-field approximation presumed with the use of 1. order methods in the data analysis program MAGRES (Nelson, 1980; Nelson and Nave, 1981; Sagstuen et al., 2000) do not strictly apply for a coupling of this magnitude.

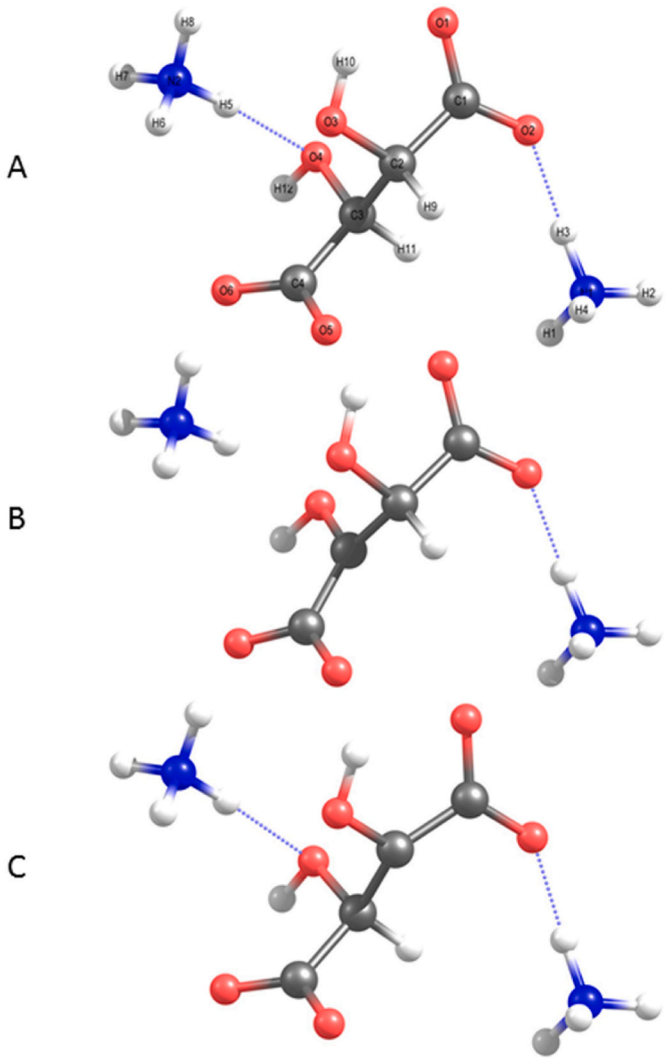

Fig. 3. Freely optimized molecular structures of (A): the diammonium tartrate molecule; (B): the radical formed by net H(C3) abstraction, model *R1-I*; and (C): the radical formed by net H(C2) abstraction, model *R1-II*; by periodic DFT calculations using a periodic cell of 16 units (384 atoms). Atomic numbering follows that shown in Fig. 1.

In the **R2** EPR spectra in partially deuterated crystals, one hyperfine interaction is missing (that is, the **R2** spectrum is a doublet of doublets), and in the corresponding ENDOR spectra, the resonance lines due to the interaction denoted **R2**(3) are absent (see Fig. S4 in the Supporting Information). Coupling **R2**(3) must therefore be due to an exchangeable proton, most probably a -$^{\bullet}$C(OH$_\beta$)- proton, as judged from the anisotropy of the coupling. Both **R2**(1) and **R2**(2) exhibit dipolar coupling tensors typical for carbon-bonded β-protons.

The EIE spectra shown in Fig. 4 and Fig. S4 (Section 4, Supporting Information) fully support the analysis presented above. An interesting feature is the asymmetry present both in the ENDOR and the EIE spectra of Fig. 4 and Fig. S4. Different intensities of the high- and low frequency

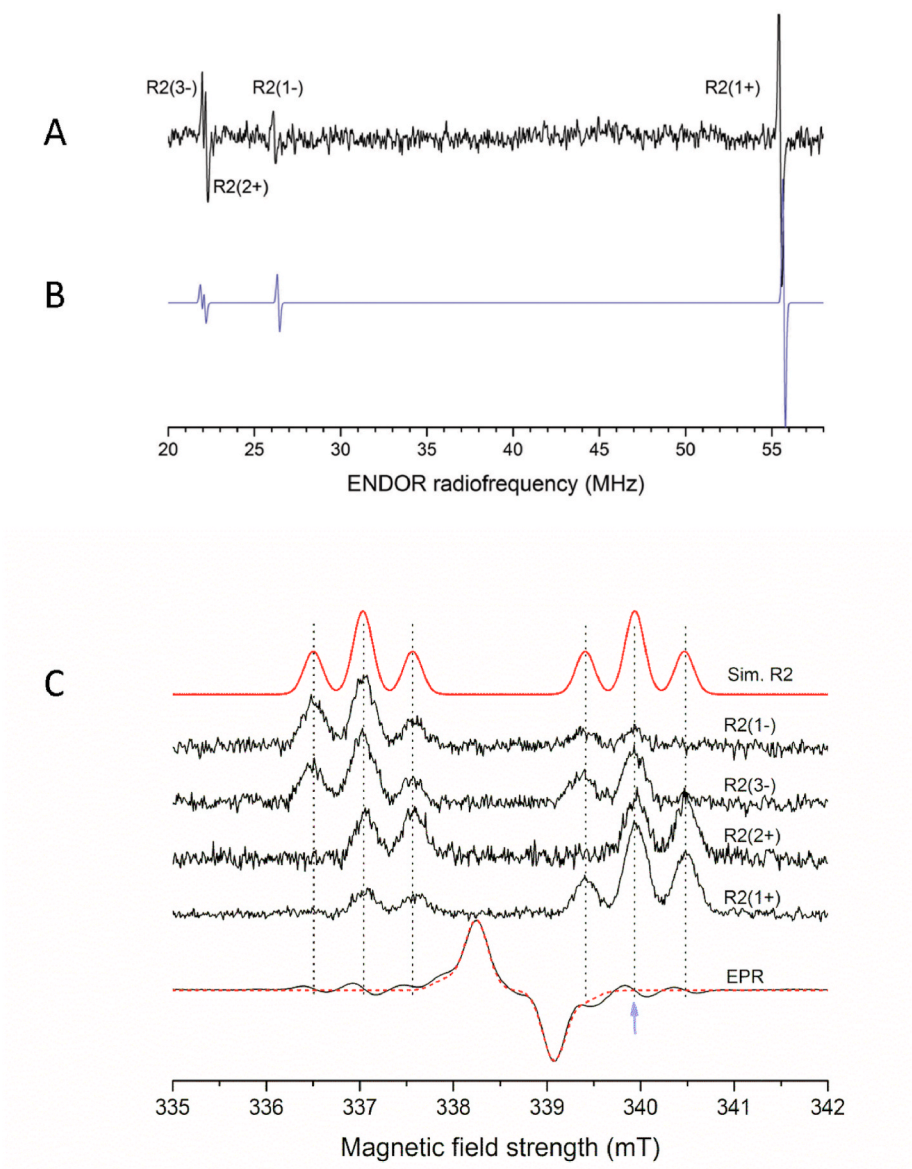

Fig. 4. EPR, ENDOR and EIE spectra from non-deutrated crystals of AT irradiated at 6 K and annealed/measured at 295 K. The external magnetic field B was directed 20° from <a> (at 110° in Supplemental Information Fig. S3, rot<b> panel) in the <c*a>-plane. The microwave frequency was 9488.2 MHz. A) The ENDOR spectrum recorded off the field position in the experimental EPR spectrum marked with an arrow in panel C. The ENDOR lines are marked in correspondence with the hyperfine coupling tensor designations in Table 3. B) EasySpin exact simulation of the ENDOR spectrum in the range 20–60 MHz, using the hfc tensor data in Table 3. See text for details. C) The top trace shows the simulated **R2** EPR spectrum in absorption mode mimicking the experimental **R2** radical EIE spectra. The bottom stippled trace shows the simulated R1 radical EPR spectrum in 1.derivative mode overlaid the experimental **R1**+**R2** radical EPR spectrum. The intermediate **R2**-radical EIE spectra are recorded off the corresponding ENDOR lines in panel A. For the low-frequency ENDOR line R2(1-) the rf was swept in opposite direction to the magnetic field (see text). Vertical dotted lines are for visual aid only.

resonance lines for a given coupling (e.g. **R2**(1+)/**R2**(1-)) are commonly observed due to hyperfine enhancement of ENDOR transition probabilities, an effect also included in the EasySpin simulation toolbox. Less common are the asymmetries observed in the EIE spectra. This type of asymmetry is ascribed to enhanced electron-nuclear cross-relaxation times for the spin system, often due to the dynamics of the spin system (Brustolon et al., 1986). This effect was previously clearly demonstrated in crystals of the amino acids alanine and glycine (Sagstuen et al., 1997; Sanderud and Sagstuen, 1998).

The g-tensor for radical **R2** could not be well determined from the EPR data, however, the available data indicates that the g-values are in the range [2.0050, 2.0026] with a maximum value close to the a-axis.

3.4. Possible models for radical R2

The EPR spectra and the data in Table 3 suggest that the major interactions for the unpaired electron are with two non-exchangeable carbon-centered β-protons and one exchangeable proton. Considering the anisotropy of the latter coupling it is most probably due to a β-OH proton. The absence of any highly anisotropic α-coupling is evident both in the EPR and the ENDOR spectra. It was first looked for possible structures assuming minimal reorganizations and excluding dimerization processes. Within these assumptions, the presence of two non-exchangeable β-protons indicates that the basic molecular backbone must be intact. Furthermore, it appears that the major spin density must be localized at C2 as the eigenvector for the major β-coupling (R2(1)) deviates only 7.5° from the crystallographic C2-HC3–direction. In addition, the eigenvector for the maximum β-OH coupling (**R2**(3)) is close to the crystallographic C2-HOC2 direction. However, based on a C2-centered radical model, the data in Table 3 do not provide any immediate match for the **R2**(2) non-exchangeable β-coupling.

Various radical products may result from primary species in the reduction and oxidation chain of events of tartaric acids, as outlined in our previous work on the Rochelle salt (Sagstuen et al., 2012; Samskog et al., 1979). Singly and doubly protonated reduced species (anions) usually are unstable at room temperature (see below) and decay by participation into various sequences of reaction processes. Possible end-products may be radical **R1** and the products (I) and (II):

$^{-}$OOC–$^{\bullet}$CH–CH(OH)–COO^{-} (I)

O=$^{\bullet}$C–CH(OH)–CH(OH)–COO^{-} (II)

Neither (I) nor (II) is compatible with the available data for **R2**. (I) is associated with a large α-coupling and the acyl radical (II) is known to be unstable at room temperature. In addition, σ-radicals like (II) exhibit g-tensors incompatible with the available data for **R2** (McCalley and Kwiram, 1970a, b; Sagstuen and Skjærvø, 1981).

In the oxidation chain, decarboxylation occurs as the C–C bond weakens upon one-electron loss from a carboxyl group. Decarboxylated products may enter intermolecular reactions. A common simple process is H-abstraction from a neighboring molecule resulting in a radical structure like **R1**. Also a product like (III) may be envisaged:

$$(O{=})CH{-}{}^{\blacksquare}C(OH){-}CH(OH){-}COO^{-} \quad \text{(III)}$$

However, similar allylic-type products were observed in e.g. sucrose, denoted radical T1 and radical T4 (De Cooman et al., 2009; Kusakovskij et al., 2017) and exhibit magnetic parameters incompatible with those for **R2**.

If more severe reorganizations are considered, including disproportionation and/or dimerization processes, several possibilities may be considered. In the current work, the lack of firm experimental data in the temperature region between 6 and 295 K prohibit most attempts to arrive at a final structure for **R2**.

3.5. DFT-calculations - protonated anions

Our preliminary low-temperature experimental EMR data did clearly indicate that the singly protonated C1-centered radical anion was present as a dominant component of the data obtained by irradiation and measurements at 6 K (see Section 5, Supplemental Information). The ENDOR based data for the major coupling from this species is presented in Table S4 (Section 5, Supplemental Information). There is also evidence available for the stabilization of the decarboxylated cation at 6 K.

Detailed periodic DFT calculations were made for all singly protonated anions of the AT one-electron reduced species. The protonation sites considered were O1, O2, O5 and O6 and the source of the proton was in each instance taken to be a transfer of a proton along the hydrogen bond from a neighboring ammonium ion donor. Two of the calculations (protonation at O1 and O6) never converged. Neither of the other two (protonation at O2 or O5, being C1- and C4-centered, resp.) yielded results compatible with the experimental data for radical **R2**. On the other hand, the DFT calculation on the O2-protonated anion showed an exceptionally good agreement with our preliminary experimental data for the O2-protonated anion in Table S4 (Section 5, Supplemental information) observed in AT at 6 K. The unconstrained DFT-calculated structure is shown in Fig. S5 (Section 5, Supplemental Information). The calculational results for both the O2 and O5 protonated anions are presented in Table S5 (Section 5, Supplemental Information).

Doubly protonated anions may still be possible structures, or precursors, for the **R2** radical. However, our calculations on doubly protonated anions all failed to converge under the calculational regime described in Section 2, suggesting them to be unstable entities which, if formed at all, immediately transform into new products by e.g. (1,2) or (1,4) type β-elimination of water, by disproportionation or otherwise.

3.6. Mechanistic considerations

In our previous work on the Rochelle salt, i.e. the (Na^+, K^+) salt of tartaric acid a reaction scheme for carboxylic acids, including the dicarboxylic acids, was proposed, based on a review of the literature as well as the new experimental data presented in that work (Sagstuen et al., 2012). Decarboxylation of the one-electron loss radical and protonation of the one-electron gain radical are the two major primary products in the oxidation and reduction chains of processes, respectively. With these two starting points, radical **R1** may be formed in both branches *via* intermolecular reactions. The present data for the one-electron O2-protonated anion in AT suggest that radical **R1** results from the reduction pathway. Our preliminary low-temperature data furthermore indicates the presence of the decarboxylated radical in AT at 6 K.

4. Conclusions

In the present work the room temperature radical formation in diammonium tartrate crystals has been reinvestigated using EPR, ENDOR, EIE and DFT methods. It has been shown that the dominant radical (**R1**) of dosimetric interest is a species formed by a net H-abstraction from the C3 carbon atom of the tartrate backbone. This reassignment of the radical structure as compared to previous analyses (Brustolon et al., 1996) has no influence on the use of AT as a radiation dosimeter. It has further been demonstrated that a second radical (**R2**) is stabilized at room temperature. Even if the experimental data for this species are comprehensive, a definitive structural assignment could not be made. The major proton coupling characterizing radical **R2** (i.e. the largest doublet splitting) is sufficiently large for the resonance spectrum of this defect not to overlap the major resonance used for dosimetry purposes to any significant degree Preliminary low temperature measurements indicate that a protonated anion radical and a decarboxylated cation radical are the most prominent primary radicals formed.

Funding

This research did not receive any specific grant from external funding sources in the public, commercial, or not-for-profit sectors.

Declaration of competing interest

The authors declare that they have no known competing financial interests or personal relationships that could have appeared to influence the work reported in this paper.

Acknowledgements

We are indebted to the initial early low-temperature work on ammonium tartrate in our labs by Dr. Tor Arne Vestad. Dr. Siv Gundrosen Aalbergsjø gave valuable advises with respect to DFT calculations. Mr. Efim Brondz as usual provided excellent technical assistance. The computational work was performed on the Abel cluster owned by the University of Oslo and the Norwegian metacenter for High Performance Computing (NOTUR). VK acknowledges a travel grant from Linköping University in support for an extended stay at University of Oslo.

Appendix A. Supplementary data

Supplementary data to this article can be found online at https://doi.org/10.1016/j.radphyschem.2022.110097.

References

Adolfsson, E., Tedgren, A.C., Carlsson, G.A., Gustafsson, H., Lund, E., 2014. Optimisation of an EPR dosimetry system for robust and high precision dosimetry. Radiat. Meas. 70, 21–28.

Bartolotta, A., D'Oca, M.C., Brai, M., Caputo, V., De Caro, V., Giannola, L.I., 2001. Response characterization of ammonium tartrate solid state pellets for ESR dosimetry with radiotherapeutic photon and electron beams. Phys. Med. Biol. 46, 461–471.

Becke, A.D., 1988. Density-functional exchange-energy approximation with correct asymptotic-behavior. Phys. Rev. A 38, 3098–3100.

Bradshaw, W.W., Cadena, D.G., Crawford, G.W., Spetzler, H.A.W., 1962. The use of alanine as a solid dosimeter. Radiat. Res. 17, 11–21.

Brustolon, M., Cassol, T., Micheletti, L., Segre, U., 1986. Methyl dynamics studied by ENDOR spectroscopy: a new method. Mol. Phys. 57, 1005–1014.

Brustolon, M., Maniero, A.L., Jovine, S., Segre, U., 1996. ENDOR and ESEEM study of the radical obtained by γ irradiation of a single crystal of ammonium tartrate. Res. Chem. Intermed. 22, 359–368.

Brustolon, M., Tampieri, F., Marrale, M., Barbon, A., 2015. Determination of new radical species in ammonium tartrate dosimeters by CW- and pulsed-EPR techniques. Appl. Magn. Reson. 46, 481–488.
Brustolon, M., Zoleo, A., Lund, A., 1999. Spin concentration in a possible ESR dosimeter: and electron spin echo study on x-irradiated ammonium tartrate. J. Magn. Reson. 137.
De Cooman, H., Pauwels, E., Vrielinck, H., Sagstuen, E., Van Doorslaer, S., Callens, F., Waroquier, M., 2009. ENDOR and HYSCORE analysis and DFT-assisted identification of the third major stable radical in sucrose single crystals X-irradiated at room temperature. Phys. Chem. Chem. Phys. 11, 1105–1114.
Godbout, N., Salahub, D.R., Andzelm, J., Wimmer, E., 1992. Optimization of Gaussian-type basis-sets for local spin-density functional calculations. 1. Boron through neon, optimization technique and validation. Can. J. Chem. 70, 560–571.
Goedecker, S., Teter, M., Hutter, J., 1996. Separable dual-space Gaussian pseudopotentials. Phys. Rev. B 1703–1710.
Gustafsson, H., Olsson, S., Lund, A., Lund, E., 2004. Ammonium formate, a compound for sensitive EPR dosimetry. Radiat. Res. 161, 464–470.
Hansen, J.W., Olsen, K.J., Wille, M., 1987. The alanine radiation detector for high and low-LET dosimetry. Radiat. Protect. Dosim. 19, 43–47.
Hartwigsen, C., Goedecker, S., Hutter, J., 1998. Relativistic separable dual-space Gaussian pseudopotentials from H to Rn. Phys. Rev. B 3641–3662.
Heydari, M.Z., Malinen, E., Hole, E.O., Sagstuen, E., 2002. Alanine radicals. 2. The composite polycrystalline alanine EPR spectrum studied by ENDOR, thermal annealing, and spectrum simulations. J. Phys. Chem. 106, 8971–8977.
Ikeya, M., 1993. New Applications of Electron Spin Resonance. Dating, Dosimetry and Microscopy. World Scientific, Singapore.
Krack, M., 2005. Pseudopotentials for H to Kr optimized for gradient-corrected exchange-correlation functionals. Theor. Chem. Acc. 114, 145–152.
Krack, M., Parrinello, M., 2000. All-electron ab-initio molecular dynamics. Phys. Chem. Chem. Phys. 2, 2105–2112.
Krivokapic, A., Sanderud, A., Aalbergsjo, S.G., Hole, E.O., Sagstuen, E., 2015. Lithium formate for EPR dosimetry (2): secondary radicals in X-irradiated crystals. Radiat. Res. 183, 675–683.
Kusakovskij, J., De Cooman, H., Sagstuen, E., Callens, F., Vrielinck, H., 2017. On the identity of the last known stable radical in X-irradiated sucrose. Chem. Phys. Lett. 674, 6–10.
Lee, C.T., Yang, W.T., Parr, R.G., 1988. Development of the Colle-Salvetti correlation-energy formula into a functional of the electron-density. Phys. Rev. B 37, 785–789.
Lippert, G., Hutter, J., Parrinello, M., 1999. The Gaussian and augmented-plane-wave density functional method for ab initio molecular dynamics simulations. Theor. Chem. Acc. 103, 124–140.
Lund, A., Olsson, S., Bonora, M., Lund, E., Gustafsson, H., 2002. New materials for ESR dosimetry. Spectrochim. Acta 58, 1301–1311.
Lund, E., Gustafsson, H., Danilczuk, M., Sastry, M.D., Lund, A., Vestad, T.A., Malinen, E., Hole, E.O., Sagstuen, E., 2005. Formates and dithionates: sensitive EPR-dosimeter materials for radiation therapy. Appl. Radiat. Isot. 62, 317–324.
Malinen, E., 2014. EPR dosimetry in clinical applications. In: Lund, A., Shiotani, M. (Eds.), Application of EPR in Radiation Research. Springer International, Inc., Heidelberg, pp. 509–538.
Marrale, M., Brai, M., Barbon, A., Brustolon, M., 2009. Analysis of the spatial distribution of free radicals in ammonium tartrate by pulse EPR techniques. Radiat. Res. 171, 349–359.
Marrale, M., Brai, M., Triolo, A., Bartolotta, A., D'Oca, M.C., 2006. Power saturation of ESR signal in ammonium tartrate exposed to ^{60}Co γ-ray photons, electrons and protons. Radiat. Res. 166, 802–809.
McCalley, R.C., Kwiram, A.C., 1970a. Discovery of a sigma-radical in X-irradiated malonic acid. JACS 92, 1441–1442.
McCalley, R.C., Kwiram, A.C., 1970b. Role of CO bond scission in the radiolysis of crystalline carboxylic acids. J. Chem. Phys. 53, 2541–2542.
Nelson, W.H., 1980. Estimation of errors in eigenvectors and eigenvalues from magnetic resonance results by use of linear data-fitting techniques. J. Magn. Reson. 38, 71–78.
Nelson, W.H., Nave, C.R., 1981. ESR and ENDOR studies of radicals produced in hydroxyproline single crystals by x-irradiation at low temperature. J. Chem. Phys. 74, 2710–2716.
Olsson, S., Bagherian, S., Lund, E., Carlsson, G.A., Lund, A., 1999. Ammonium tartrate as an ESR dosimeter material. Appl. Radiat. Isot. 50, 955–965.
Olsson, S.K., Lund, E., Lund, A., 2000. Development of ammonium tartrate as an ESR dosimeter material for clinical purposes. Appl. Radiat. Isot. 52, 1235–1241.
Polat, M., Korkmaz, M., 2009. The effects of temperature on ESR spectrum of gamma-irradiated ammonium tartrate. Radiat. Phys. Chem. 78, 966–970.
Regulla, D.F., Deffner, U., 1982. Dosimetry by ESR spectroscopy of alanine. Appl. Radiat. Isot. 33, 1101–1114.
Sagstuen, E., Hole, E.O., Haugedal, S.R., Nelson, W.H., 1997. Alanine radicals: structure determination by EPR and ENDOR of single crystals X-irradiated at 295 K. J. Phys. Chem. A101, 9763–9772.
Sagstuen, E., Hole, E.O., Lund, A., 2012. Free radical products in X-irradiated Rochelle salt: low temperature ENDOR and DFT studies. Radiat. Phys. Chem. 81, 168–179.
Sagstuen, E., Lund, A., Itagaki, Y., Maruani, J., 2000. Weakly coupled proton interactions in the malonic acid radical: single crystal ENDOR analysis and EPR simulation at microwave saturation. J. Phys. Chem. 104, 6362–6371.
Sagstuen, E., Skjærvø, H., 1981. On the ESR detection of the sigma-radical RNHCO· in irradiated crystals of 5,5-dihydroxybarbituric acid (alloxan) trihydrate. J. Chem. Phys. 75, 5627–5629.
Samskog, P.-O., Lund, A., Nilsson, G., Symons, M.C.R., 1979. Primary reactions in crystalline salts of tartaric acids studied by EPR spectroscopy. Chem. Phys. Lett. 66, 199–202.
Sanderud, A., Sagstuen, E., 1998. EPR and ENDOR studies of single crystals of α-Glycine X-ray irradiated at 295 K. J. Phys. Chem. B 102, 9353–9361.
Schonland, D.S., 1959. On the determination of the principal g-values in electron spin resonance. Proc. Phys. Soc. 73, 788–792.
Stoll, S., Schweiger, A., 2006. EasySpin, a comprehensive software package for spectral simulation and analysis in EPR. J. Magn. Reson. 178, 42–55.
The CP2K developers group, 2011. CP2K, 2.3, p. 39. Last. http://www.cp2k.org, 01/19/2022.
VandeVondele, J., Hutter, J., 2007. Gaussian basis sets for accurate calculations on molecular systems in gas and condensed phases. J. Chem. Phys. 127, 114105.
Vestad, T.A., Gustafsson, H., Lund, A., Hole, E.O., Sagstuen, E., 2004. Radiation induced radicals in lithium formate monohydrate ($LiHCO_2{\cdot}H_2O$). EPR and ENDOR studies of X-irradiated crystal and polycrystalline samples. Phys. Chem. Chem. Phys. 6, 3017–3022.
Vestad, T.A., Malinen, E., Lund, A., Hole, E.O., Sagstuen, E., 2003. EPR dosimetric properties of formates. Appl. Radiat. Isot. 59, 181–188.
Vrielinck, H., De Cooman, H., Tarpan, M.A., Sagstuen, E., Waroquier, M., Callens, F., 2008. Schonland ambiguity in the electron nuclear double resonance analysis of hyperfine interactions: principles and practice. J. Magn. Reson. 195, 196–205.
Wieser, A., Siegele, R., Regulla, D.F., 1989. Influence of the irradiation temperature on the free-radical response of alanine. Appl. Radiat. Isot. 40, 957–959.
Yadava, V.S., Padmanabhan, V.M., 1973. The crystal structure of ammonium tartrate. Acta Crystallogr. B 29, 493–498.
Yadava, V.S., Padmanabhan, V.M., 1976. Neutron diffraction study of ammonium tartrate $(NH_4)_2C_4H_4O_6$. Pramana 6, 94–101.